# USING ABAQUS TO SIMULATE THE TRIAXIAL STRESS STRAIN BEHAVIOR OF CORE SAMPLES FROM THE WAIRAKEI/TAUHARA GEOTHERMAL FIELD

Justin Pogacnik*[1], Wesley Koros[1], John O'Sullivan[1], Michael Pender[2], Mike O'Sullivan[1], Chris Bromley[3]

[1] Department of Engineering Science, University of Auckland, Level 3 70 Symonds St Auckland 1142, New Zealand

[2] Department of Civil and Environmental Engineering, University of Auckland, Level 11 20 Symonds St Auckland 1142, New Zealand

[3] GNS Science, Wairakei Research Centre, Private Bag 2000, Taupo, 3352, New Zealand

*j.pogacnik@auckland.ac.nz

**Keywords:** *Wairakei subsidence, Cam-clay model, finite element method, triaxial testing*

## ABSTRACT

The Wairakei geothermal field in New Zealand has experienced a significant amount of production related subsidence in the last 50 years. Therefore, the region has been subject to a significant amount of data collection and rock characterization work. However, the rock properties associated with mechanical deformation are often overly simplified in numerical simulations of subsidence. We seek to calibrate an advanced elastic-plastic constitutive relationship (Modified Cam-clay) to rock data from $K_0$ triaxial tests on core samples from geotechnical reports of the field. We do this by setting up radially symmetric finite element simulations using the software ABAQUS to closely match the triaxial laboratory tests. The parameterized Cam-clay models will be applied as future work in our development of a more realistic numerical subsidence model of the Wairakei geothermal field.

## 1. INTRODUCTION/BACKGROUND

### 1.1 Subsidence at Wairakei/Tauhara

Geothermal exploitation of the Wairakei geothermal field has clearly been the cause of major ground subsidence (Hatton (1970)). In fact, there has been more fluid-withdrawal related subsidence in parts of the Wairakei field than any other development (geothermal or otherwise) in the world (Allis (2000)). Hatton (1970) is credited with the first publication documenting subsidence in the Wairakei geothermal field. However, Hatton stated that the first indications of subsidence were seen as early as 1956 when elevation discrepancies were found from several benchmark points in the area. One such comparison (benchmark A97) indicated nearly 8 cm of subsidence had occurred in the eastern Wairakei field since the previous 1950 levelling survey. The rate of subsidence of the Wairakei field continued to increase through the 60s and 70s reaching a peak of about 50 cm/year in 1978 (Koros, et al. (2014)). Allis (2000) reported that the total subsidence at the center of the Wairakei subsidence bowl was approximately 14 m in 1997 and that it could reach 20 m by 2050. A levelling survey performed from 2004 - 2009 found that subsidence rates within main Wairakei bowl (centred in Wairakei Thermal Valley) declined to a maximum of 5 cm/yr (see Bromley, et al. (2013)) resulting in a total subsidence of 15 m (Allis, et al. (2009)).

### 1.2 Previous Modelling Work

There have been a number of studies seeking to characterise the subsidence in Wairakei through numerical modelling. Many can trace their roots back to Geertsma's (1973) derivation of an expression for 1D subsidence in a theoretical half-space. Geertsma's formulation relies on the successful characterisation of the compaction coefficient, a material parameter related to the elastic properties of the material. Herd (1985) was perhaps the first to create a numerical subsidence model for Wairakei and utilised the finite element method. That work consisted of 2D simulations that included the pumice breccia overburden and Huka Falls formation with increasing effective stress as a result of production. Allis and Zhan (2000) utilised a quasi-1D column model to simulate the subsidence history of Wairakei. Their work coupled solid mechanics to fluid flow through Biot's effective stress formulation in a finite element code developed by Schrefler and co-workers (Lewis and Schrefler (1998) and Schrefler and Zhan (1993)). They used a simplified 2 layer model similar to Herd (1985) and varied the linear elastic rock properties to match the subsidence history. Lawless, et al. (2001) and White, et al. (2005) also developed subsidence models of the Wairakei field using the software package, Plaxis. They performed 2D simulations that accounted for different geological strata in the area. They adjusted material properties within geological units in order to match the subsidence history of the field. Yeh and O'Sullivan (2007) linked the solid mechanics package, ABAQUS, to the reservoir simulator, Tough2, in order to perform 3D subsidence simulations of the Wairakei field. They expressed a need to improve the shallow pressures of the Tough2 reservoir model in order to accurately match the time evolution of the subsidence. All the authors mentioned in this section expressed a desire for more rock property characterisation data in order to better calibrate the solid constitutive behaviour.

### 1.3 Experimental Rock Characterisation

In order to quantify the rock properties in the area, an extensive program of drilling, coring, and scientific investigations was undertaken from 2007-2009 by Contact Energy, Ltd. (Bromley, et al (2010); Bromley, et al (2013)). An approximate total of 4 km of core samples were collected for testing. $K_0$ triaxial testing was performed to determine material stiffness. Other mechanical tests performed were point load stength, pocket penetrometer strength, shear vane undrained strength, density, water content, porosity, Atterberg limits, particle size distribution, smectite content, relative clay abundance, and scanning electron microscopy.

The laboratory-derived stress strain curve is one of the most useful results for calibrating numerical solid constitutive models to data. The setup and results of the laboratory $K_0$ triaxial tests are reported in Laboratory testing of core from the Wairakei-Tauhara geothermal field – Factual Procedures Report and Interpretive Procedures Report, Appendices 8 and 9 (Pender (2010a,b;2013)).

### 1.4 Current Modelling Effort

This work seeks to calibrate an elastic-plastic solid constitutive model (Modified Cam-clay) in ABAQUS to core data from $K_0$ triaxial test data. The results from these calibrations are applied in a pseudo 1D subsidence model being developed by Koros and co-workers (Koros, et al (2014); Koros, et al (2015)). These works are part of a more recent effort at the University of Auckland to model subsidence at Wairakei. The ultimate goal of the current modelling effort is to incorporate subsidence into the reservoir-scale 3D simulations. Currently, we are seeking to understand and implement as many of the known rock properties as possible from the before mentioned subsidence reports in 1D subsidence models to maximise the utility of the simple 1D case. This includes investigating the application of a constitutive relationship for cohesive soil, modified Cam clay, to the behaviour of very weak rock.

In this work, we present the governing balance equations for a thermal-poroelastic stress analysis, then present the basics of plasticity theory. Plasticity theory builds to a particular model designed for clays, but appropriate for very soft rocks, the modified Cam-clay model. Finally, we will present our calibration of the Cam-clay model to one triaxial test from the Wairakei/Tauhara area performed by Pender, et al (2009a,b). We then perform a parameter study on the model parameters that require calibration to determine their effect on the stress-strain response of the compressed material. This is an important study required for our future 1D and 3D subsidence modelling efforts. This paper finishes with a summary and conclusions.

## 2. BALANCE EQUATIONS FOR ROCK MATRIX

In this work, inertial forces in the solid rock matrix were ignored. The linear momentum balance from Bonet and Wood (2008) is written as:

$$\operatorname{div} \boldsymbol{\sigma} + \boldsymbol{f} = \mathbf{0} \tag{1}$$

where the vector $\operatorname{div} \boldsymbol{\sigma}$ is the spatial divergence of the Cauchy stress tensor and $\boldsymbol{f}$ a vector of body forces (both external and density related). Note that boldface fonts are used to express matrix and vector quantities. We use standard engineering convention here so that stress is positive in tension and negative in compression. The Cauchy stress can be split into two components to represent the effect of pore fluid pressure on the solid matrix (Lewis and Schrefler (1998); Ingebritsen, Sanford, and Neuzil (2006)):

$$\boldsymbol{\sigma} = \boldsymbol{\sigma}' - \alpha p \mathbf{I} \tag{2}$$

where $\boldsymbol{\sigma}'$ is Biot's effective stress tensor, $\alpha$ is a constant between 0 and 1, $p$ is the pore fluid pressure, and $\mathbf{I}$ is the identity tensor. The constant $\alpha$ was set to 1 in this work as per the analysis of Pender et al. (2013). The effective stress is defined in terms of strain by Hooke's law:

$$\boldsymbol{\sigma}' = \mathbf{C}^{\mathrm{e}} : (\boldsymbol{\varepsilon} - \boldsymbol{\varepsilon_T}) \tag{3}$$

where $\mathbf{C}^{\mathrm{e}}$ is the fourth order material constitutive tensor, $\boldsymbol{\varepsilon}$ is the strain tensor, ":" represents the double contraction of two tensors, and $\boldsymbol{\varepsilon}_T$ is the thermal strain tensor given by

$$\boldsymbol{\varepsilon}_T = \left(\frac{\beta_{\mathrm{s}}}{3}\right)(\Delta T)\,\mathbf{I} \tag{4}$$

where $\beta_{\mathrm{s}}$ is the volumetric coefficient of thermal expansion of the solid and $\Delta T$ is the change in temperature from the reference state. For completeness, the fourth order elasticity tensor can be defined (in indicial notation):

$$\mathrm{C}^{\mathrm{e}}_{ijkl} = \left(K - \frac{2}{3}G\right)\delta_{ij}\delta_{kl} + G\left(\delta_{ik}\delta_{jl} + \delta_{il}\delta_{jk}\right) \tag{5}$$

where $\delta_{ij}$ is the Kronecker delta equal to 1 when $i = j$ and 0 when $i \neq j$, $K$ is the bulk modulus, and $G$ is the shear modulus.

The triaxial tests from Pender, et al (2010a,b) were run in such a way that the pore fluid pressure and temperature could be taken as uniform and constant throughout the domain during a test. Therefore, we ignore heat and mass transfer in this work, but still consider pressure and temperature effects in a thermal poroelastic stress analysis by applying equations (1) - (4).

## 3. MODIFIED CAM-CLAY CONSTITUTIVE MODEL

Cam-clay is the name given to a particular elastic-plastic model for describing soil behaviour. The model was originally developed by Roscoe and Schofield (1963). However, Roscoe and Burland (1968) developed the more commonly used version termed *modified* Cam-clay. A companion paper (Koros, et al. (2015)) shows that the soft layers of the Wairakei/Tauhara field that are predominantly responsible for subsidence can be considered as clay-like materials. Therefore, that work provides the justification for use of the Cam-clay constitutive model. This section seeks to introduce plasticity and outline the relevant modified Cam-clay details for this work.

### 3.1 Elasticity and Plasticity

Elastic materials exhibit a one to one relationship between stress and strain, called Hooke's Law. The law is named after Robert Hooke who first published the force-extension relationship in 1675 (Wood (1990)). The relationship (seen graphically in Figure 1) can be linear (1(a)) or nonlinear (1(b)), but the important feature is that upon unloading, the material returns to an initial stress and strain free state with no net energy dissipation (Wood (1990)).

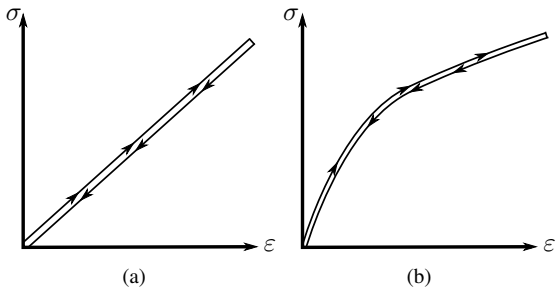


**Figure 1: Example of linear (1(a)) and nonlinear (1(b)) elastic stress-strain relationships (after Wood (1990)).**

Many materials are not well described by an elastic relationship. The theory of plasticity offers a necessary extension to elastic theory and is concerned with the analyses of stresses and strains in a material in the plastic region as well as the elastic region. Figure 2 shows an example of an elastic-plastic material during loading and subsequent unloading/loading cycles. After initial loading, the stress is removed from the material at point $A$. The material unloads along a different path and then reloads along the unloading path if loading is resumed. Notice that at point $B$, the stress has been removed, but some strain/deformation remains. The distance from the origin to point $B$ represents the plastic strain.

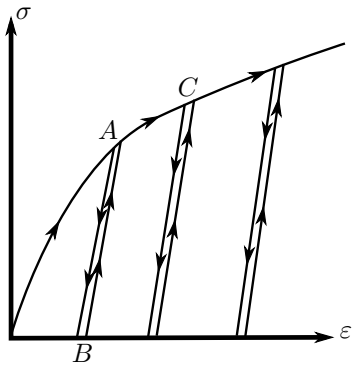


**Figure 2: An example of loading/unloading behaviour of an elastic-plastic material.**

The term *yield* is used to describe the onset of plastic strain/deformation. Tresca is credited with proposing the first yield condition in the 1860s (Chen and Han (1995)). A yield condition is a requirement for plasticity theory. Perhaps the most common yield condition is the von Mises condition or $J_2$ condition, which is related to the second invariant of the deviatoric stress tensor:

$$J_2 = \frac{1}{6}\left[(\sigma_1 - \sigma_2)^2 + (\sigma_2 - \sigma_3)^2 + (\sigma_3 - \sigma_1)^2\right] \quad (6)$$

where $\sigma_i$ are the principal stresses of the Cauchy stress tensor. When the second stress invariant exceeds a critical value of $J_2$, yielding occurs and is controlled by an appropriate *flow rule* from a *plastic potential function*.

The flow rule is simply a function that determines the plastic strain tensor after yielding occurs. The flow rule can be derived from a plastic potential function:

$$d\boldsymbol{\varepsilon}^p = d\Lambda \left(\frac{\partial g}{\partial \boldsymbol{\sigma}}\right) \quad (7)$$

where $\boldsymbol{\varepsilon}^p$ is the plastic strain tensor, $d\Lambda$ is a positive scalar of proportionality which is only nonzero when plastic deformation occurs, and $g$ is the plastic potential function similar to the strain energy density function of elasticity theory. If $g$ is related to the yield condition, the flow rule is called an *associated* flow rule. If $g$ is not related to the yield condition, the flow rule is called a *nonassociated* flow rule.

Figure 2 shows that work hardening occurs after the onset of yield. Notice how the stress increases from point $A$ to point $C$. A rule that characterises work hardening is the last major component required for plasticity theory. Hardening is typically conceptualised in principal stress space. Figure 3 displays the 2D principal stress space. The dashed line ellipse in the centre represents the initial yield surface or the yield stress ($\sigma_{\mathrm{Y0}}$) by the von Mises condition of equation (6). When a material is deformed plastically, the yield surface expands (isotropic hardening) and/or translates (kinematic hardening) as seen by the updated yield surface ($\sigma_{\mathrm{Y}}$) given by the solid line ellipse. The transition from the dashed line ellipse to the solid line ellipse could be representative of the stress/strain progression from point $A$ to point $C$ in Figure 2. All material behaviour inside the current yield surface (solid line) is elastic in nature.

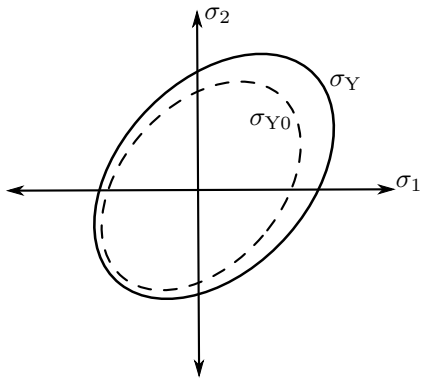


**Figure 3: Initial (dashed line) and subsequent (solid line) yield surfaces for a work hardened material due to a combination of isotropic and kinematic hardening.**

In this section, we have outlined the four fundamentals of plasticity theory as described by Wood (1990) and Chen and Han (1995). Those fundamentals are elasticity theory, yield properties, plastic potential and flow rule, and hardening rule. The next section will seek to develop the relevant details of these fundamentals for the modified Cam-clay plasticity model.

### 3.2 Development of the Modified Cam-clay Model

#### 3.2.1 Elastic Behaviour

The next two sections closely follow Chapter 5 in Wood (1990). However, the reader may notice some sign convention differences as we adopt standard engineering sign convention (positive = tension, negative = compression) and Wood uses the opposite. Linear elasticity is typically used for the elastic portion of the elastic-plastic modified Cam-clay model. The modified Cam-clay model is typically described in terms of effective stress quantities. Those quantities are $p'$ (effective mean stress) and $q$ (deviator stress or von Mises stress). The effective mean stress is defined as the average of the trace of the effective stress tensor:

$$p' = -\frac{1}{3}\left(\sigma_1' + \sigma_2' + \sigma_3'\right) \quad (8)$$

The deviator stress is given by:

$$q = \sqrt{\frac{3}{2}\mathbf{S} : \mathbf{S}} = \sqrt{3\,J_2} \quad (9)$$

where $\mathbf{S}$ is the standard deviatoric stress tensor given by:

$$\mathbf{S} = \boldsymbol{\sigma} - \frac{1}{3}\mathrm{tr}(\boldsymbol{\sigma})\mathbf{I} \quad (10)$$

Also of importance is the specific volume – the volume composed of a unit volume of solid particles with their surrounding voids:

$$\mathcal{V} \equiv \frac{V_T}{V_S} = \frac{1}{1-n} = 1 + e \quad (11)$$

where $V_T$ is the total volume of solids and voids combined, $V_S$ is the volume of solids, $n$ is porosity, and $e$ is the void ratio.

The basic volumetric material behaviour of the Cam-clay model can be summarised in a plot of the mean effective stress vs specific volume as shown in Figure 4. This figure is analogous to the traditional stress-strain plot as shown in Figure 2. The line of steeper descent marked by slope $\lambda$ is called the normal consolidation/virgin compression line. It describes the plastic behaviour of the material and is linked to the material's

hardening behaviour. The parameter $N$ is a constant for a particular soil and represents the specific volume when $\ln(p') = 0$ (or $p' = 1$). The parallel lines of a lesser slope $\kappa$ represent unloading-reloading lines and the elastic behaviour of the material. The equations of the unloading-reloading lines are (in general):

$$\mathcal{V} = \mathcal{V}_\kappa - \kappa \ln(p') \tag{12}$$

because

$$\frac{d\ln(p')}{dp'} = \frac{1}{p'} \tag{13}$$

The equation can be recast in incremental form when $\kappa$ is taken as a constant as:

$$\delta\mathcal{V}^e = -\kappa\frac{\delta p'}{p'} \tag{14}$$

where the superscript $e$ indicates that the material is elastic. Lastly, by definition

$$\delta\varepsilon_v \equiv -\frac{\delta\mathcal{V}}{\mathcal{V}} \tag{15}$$

where the negative is due to the sign difference between engineering and geomechanics sign conventions and $\varepsilon_v$ is the volumetric strain given by

$$\varepsilon_v = \mathrm{tr}(\boldsymbol{\varepsilon}) \tag{16}$$

Finally, equation (14) can be rewritten in terms of incremental volumetric strain:

$$\delta\varepsilon_v^e = \kappa\frac{\delta p'}{\mathcal{V}\, p'} \tag{17}$$

This equation is consistent with the volumetric deformation of linear elasticity and fundamental to the development of the Cam-clay model. The parameter $\kappa$ is called the *logarithmic bulk modulus* and is defined on a natural log scale. Therefore, in linear stress-strain space, the Cam-clay model will present hardening behaviour in the elastic portion of the stress strain curve. That is, the slope of the stress-strain line will increase with increasing strain. This is not necessarily a requirement, as linear elasticity can also be used in the elastic portion of the stress strain curve. Similarly to equation (17), an expression exists relating the shear strain increment to the deviator stress:

$$\delta\varepsilon_q^e = \frac{\delta q}{3G} \tag{18}$$

where $\varepsilon_q$ is the second invariant of the deviatoric strain tensor, defined in the same way as the deviator stress from equations (9) and (10).

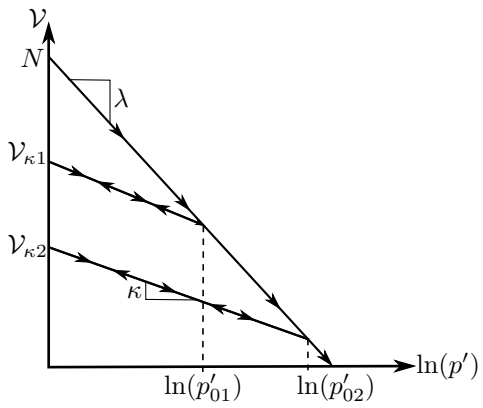


**Figure 4: Normal compression line and loading/unloading line in $\mathcal{V} - \ln(p')$ space.**

### 3.2.2 Plastic Behaviour

Having developed the elastic volumetric behaviour of the modified Cam-clay model, our discussion now moves to the plastic behaviour associated with yield. The increment of total strain can be decomposed into elastic and plastic components where each of those can be decomposed into volumetric and deviatoric components. Figure 5 displays the Cam-clay yield surface (or locus) at a specific loading point as the dashed ellipse in $p' - q$ or equivalently $\delta\varepsilon_v - \delta\varepsilon_q$ space. The modified Cam-clay model has an associated flow rule, so the plastic potential ($g$) is related (equivalent in this case) to the yield function $f$. The equation of the yield ellipse is given by:

$$g = f = q^2 - M^2\left[p'\left(p'_0 - p'\right)\right] = 0 \tag{19}$$

where $M$ controls the shape and $p'_0$ controls the size of the ellipse. Notice that the ellipse passes through the origin. The assumption is that clay materials cannot support tension. Therefore, anything left of the $q$ axis is negative mean effective stress and in tension. Tensile behaviour represents failure in a Cam-clay material. After yield, the new yield surface is represented by the solid ellipse, with an updated $p'_0$. Expansion of the yield surface always occurs in the normal direction to the previous yield surface (as seen in Figure 5). When yielding has occurred, the incremental increase of $p'_0$ can be computed through the following relation:

$$\frac{\delta p'_0}{p'_0} = \left(\frac{M^2 - \eta^2}{M^2 + \eta^2}\right)\frac{\delta p'}{p'} + \left(\frac{2\eta}{M^2 + \eta^2}\right)\frac{\delta q}{p'} \tag{20}$$

where $\eta = q/p'$.

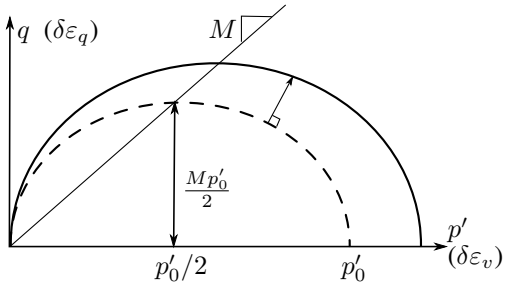


**Figure 5: Elliptical yield loci for the modified Cam-clay model in the $p' - q$ space.**

The magnitude of the volumetric plastic strain increase during yielding can be determined in a similar manner to the previous section where equation (17) gave the increment of volumetric elastic strain. Figure 4 shows that the irrecoverable change in volume over that loading history from $p'_{01}$ to $p'_{02}$ is simply the difference between the two $\mathcal{V}$ values of the loading/unloading lines:

$$\Delta\mathcal{V}^p = \mathcal{V}_{\kappa 1} - \mathcal{V}_{\kappa 2} \tag{21}$$

The equations for the intersection of the loading/unloading lines with the normal consolidation line at those $p'_0$ values can be written as:

$$\mathcal{V}_{\kappa 1}(p'_{01}) = N - \lambda\ln(p'_{01}) = \mathcal{V}_{\kappa 1} - \kappa\ln(p'_{01}) \tag{22}$$

and

$$\mathcal{V}_{\kappa 2}(p'_{02}) = N - \lambda\ln(p'_{02}) = \mathcal{V}_{\kappa 2} - \kappa\ln(p'_{02}) \tag{23}$$

Substitution of these expressions into (21) gives:

$$\begin{aligned}\Delta\mathcal{V}^p &= N - \lambda\ln(p'_{02}) + \kappa\ln(p'_{02}) \\ &- N + \lambda\ln(p'_{01}) - \kappa\ln(p'_{01})\end{aligned} \tag{24}$$

Solving in the limit and dividing by the specific volume yields the plastic strain increment:

$$\delta\varepsilon_v^p = (\lambda - \kappa)\,\frac{\delta p_0'}{\mathcal{V}\,p_0'} \tag{25}$$

Because the expansion of the yield surface is always normal in Figure 5, the deviatoric strain increment can be found by:

$$\frac{\delta\varepsilon_v^p}{\delta\varepsilon_q^p} = \frac{\partial g/\partial p'}{\partial g/\partial q} = \frac{M^2 - \eta^2}{2\eta} \tag{26}$$

The theoretical development of modified Cam-clay is complete at this point. To finish we present two matrix system of equations that can be used to relate the increment of effective mean stress and deviatoric stress to the increment of elastic and plastic volumetric and deviatoric strains (from Wood (1990)):

$$\begin{bmatrix}\delta\varepsilon_v^e \\ \delta\varepsilon_q^e\end{bmatrix} = \begin{bmatrix}\kappa & 0 \\ 0 & 1/(3G)\end{bmatrix}\begin{bmatrix}\delta p' \\ \delta q\end{bmatrix} \tag{27}$$

and

$$\begin{bmatrix}\delta\varepsilon_v^p \\ \delta\varepsilon_q^p\end{bmatrix} = \frac{\lambda - \kappa}{\mathcal{V}p'\,(M^2 + \eta^2)}\begin{bmatrix}M^2 - \eta^2 & 2\eta \\ 2\eta & 4\eta^2/(M^2 - \eta^2)\end{bmatrix}\begin{bmatrix}\delta p' \\ \delta q\end{bmatrix} \tag{28}$$

### 3.2.3 The Critical State Line

The Cam-clay model is based on the *critical state* condition. That is, under deformation, clay-like materials tend toward an ultimate condition in which plastic shear deformation continues indefinitely without changes in volume or effective stress, i.e.,

$$\frac{\partial p'}{\partial \varepsilon_q} = \frac{\partial q}{\partial \varepsilon_q} = \frac{\partial \mathcal{V}}{\partial \varepsilon_q} = 0 \tag{29}$$

This happens at a critical (subscript $c$) stress ratio:

$$\frac{q_c}{p_c'} = \eta_c \to M \tag{30}$$

where $\eta$ and $M$ are the same as the previous section and $M$ is the slope of the critical state line in Figure 5.

When plastic deformations occur, the yield locus can either expand or contract to result in either softening or hardening behaviours, respectively. Figure 6 shows this behaviour. The original yield surface of a hypothetical material is represented by the solid line ellipse in the centre. If a material is loaded from point $D$ to just beyond point $E$ to yield, the value of $\eta$ is below $M$ and the material will harden by enlarging the ellipse and $p_0'$. The material tends toward the stress state where the critical state line and the yield surface intersect at point $F$. The path represented by $DEF$ is said to be *wet* of critical. In the softening case, a material is loaded from $A$ to yield at point $B$. Since, $\eta$ is greater than $M$ in this scenario, the material softens to approach the critical state line/yield surface intersection point at $C$. The parth $ABC$ is said to be *dry* of critical. The stress strain behaviour of each of these scenarios can be seen in Figure 7.

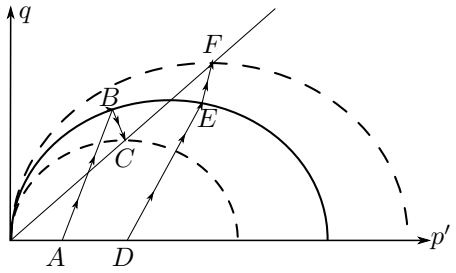


**Figure 6: Evolution of the Cam-clay yield surface for both hardening and softening behaviour based on the critical state concept.**

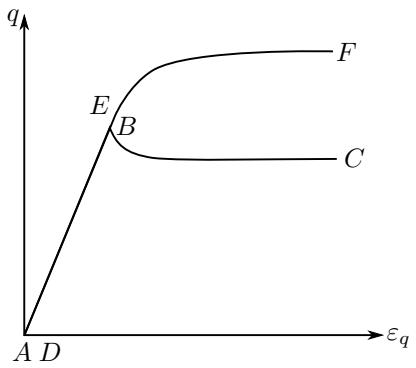


**Figure 7: Stress-strain response of Cam-clay material for both hardening and softening behaviour based on the critical state concept.**

### 3.3 Modified Cam-clay in ABAQUS

The critical state material model implemented in ABAQUS is stated in the manual as being an extension of the modified Cam-clay material model and is called through the keyword syntax: `*CLAY PLASTICITY` in the input file. The yield surface equation used in ABAQUS is:

$$f = \frac{1}{\beta^2}\left(\frac{p'}{a} - 1\right)^2 + \left(\frac{t'}{Ma}\right)^2 - 1 = 0 \tag{31}$$

where $\beta$ is a factor that determines the yield surface shape on the *wet* side of the ellipse. That is, the side of the yield surface ellipse that is *below* the critical state line. The case of $\beta = 1$ corresponds to the modified Cam-clay model described earlier and was used in this work. The ABAQUS manual states that in most cases $\beta < 1$. The other factor $a$ determines the size of the yield surface. ABAQUS offers three different options for $a$. The first two are exponential hardening rules that require the syntax: `HARDENING=EXPONENTIAL` to follow the clay plasticity keyword. In either case, the parameter $a$ is computed by

$$a = a_0 \exp\left[(1 + e_0)\frac{1 - J^p}{\lambda - \kappa\,J^p}\right] \tag{32}$$

where $e_0$ is the initial value of the void ratio on the normal consolidation line from Figure 4 (not equivalent to the intercept $N$). The parameter $a_0$ is the initial size of the yield surface and can be specified by the user. If the intercept $N$ is known, the user can specify an additional syntax on the same line: `INTERCEPT=<`$e_1$`>` where $e_1$ is found from the definition of the void ratio $N = 1 + e_1$. This is then used to compute $a_0$ from the following relationship:

$$a_0 = \frac{1}{2}\exp\left[\frac{e_1 + e_0 - \kappa \ln p_0'}{\lambda - \kappa}\right] \tag{33}$$

The parameter $J^p$ is related through the natural logarithm to the volumetric plastic strain $\varepsilon_v^p$, i.e.,

$$\varepsilon_v^p = \ln J^p \tag{34}$$

Additionally, the user can omit exponential hardening rules, by using the syntax `HARDENING=TABULAR`. This requires the extra keyword to be added on the next line: `*CLAY HARDENING`. With this option, $a$ is computed by:

$$a = \frac{p'}{1+\beta} \tag{35}$$

where the user specifies a table of $p'$ values and equivalent volumetric plastic strains $\varepsilon_v^p$ for as many data points as available. The table must start at $\varepsilon_v^p = 0$, so the initial $p'$ is equivalent to the mean effective yield stress of the material. Lastly, in the yield function, $t'$ is defined as $t' = q/g'$ where $g'$ is a function of an additional factor that affects the shape of the yield surface in principal stress space. The modified Cam-clay ellipse is recovered when $g' = 1$, so that value was used in this work. In this work, we have tested both the tabular hardening rule and the exponential hardening rule with the intercept defined. The next section will outline the calibration procedure for each hardening rule tested.

## 4. CALIBRATION OF NUMERICAL MODEL

In this study, we focused on a single core specimen recorded in the triaxial test data from Pender (2009a,b) – test 80. The sample came from a depth of about 180 m in well THM 18. The specimen was chosen because it was from a formation that potentially contributed to surface subsidence and the test showed a significant reduction in deformation resistance after yield.

### 4.1 Simulation Set Up

Simulations were set up in ABAQUS to be as near as possible to the actual $K_0$ triaxial tests performed. Figure 8 shows the meshed finite element geometry with boundary conditions. The simulations were 2D axially symmetric with the symmetry line running along the left hand side of the geometry. The bottom and right surfaces were fixed from normal displacement and vertical displacement $\Delta d$ was specified on the top surface. The specimen was dimensioned to be $3.04\,\mathrm{cm}$ wide $\times 12.0\,\mathrm{cm}$ tall to correspond to the cylinder dimensions used in the test. The geometry was discretised into 100 elements ($10 \times 10$). The temperature in the domain was fixed to $15^\circ$ C and the pore fluid pressure was fixed to be 710 kPa. The final axial strain reported for the experiment (see Figure 9) was slightly less that 3% which corresponds to about 0.36 cm vertical displacement. The simulation was run in 15 quasi-static simulations with $\Delta d = 0.03$ cm/step. This lead to a total displacement of 0.45 cm and a strain of nearly 4%.

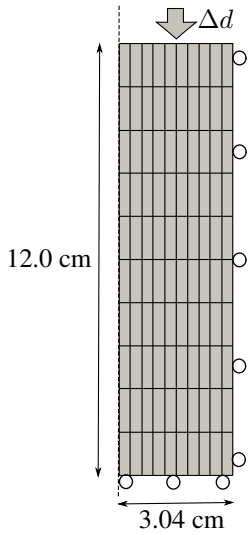


**Figure 8: Geometry with boundary conditions for $K_0$ triaxial test simulations.**

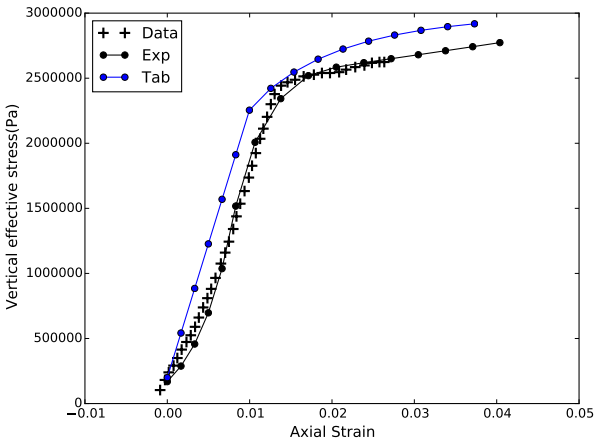


**Figure 9: Stress-strain response from $K_0$ triaxial test (Pender (2009a,b)) and calibrated numerical simulations.**

Two different versions of the modified Cam-clay constitutive model were parameterised and tested in this study. The tabular hardening option and the exponential hardening option with the intercept of the normal consolidation line defined. Figure 9 displays the calibrated axial stress-strain response for each method. It should be noted here that the purpose of this study was to determine if the modified Cam-clay work hardening framework could be used to represent some of the soft rock behaviour from the Wairakei-Tauhara area. Clearly, the framework does sufficiently capture the axial behaviour in a laboratory $K_0$ test. The next sections will detail the calibration process for each hardening model utilised.

### 4.2 Exponential Hardening

The exponential hardening model requires the use of the ABAQUS elastic model `*POROUS ELASTIC`. The input parameters for that model are the logarithmic bulk modulus ($\kappa$) and the Poisson's ratio ($\nu$). We found that it was necessary to manually adjust $\kappa$ to achieve a good fit to the test data. Poisson's ratio was reported by Pender (2009) and fixed at that value. The additional plastic parameters required were the slope of the critical state line $M$, the plastic bulk modulus or slope of the normal

consolidation line $\lambda$, and the intercept of the normal consolidation line $e_1$. $M$ can be found by solving equation (26). The increment of volumetric plastic strain can be found to be:

$$\delta\varepsilon_v^p = \delta\varepsilon_1 + \delta\varepsilon_2 + \delta\varepsilon_3 = \delta\varepsilon_1 \tag{36}$$

because for an axially symmetric problem $\delta\varepsilon_2 = \delta\varepsilon_3$. Further, for a $K_0$ triaxial test, the deformation in the radial direction is zero. Therefore, $\delta\varepsilon_2 = \delta\varepsilon_3 = 0$. The increment in deviatoric plastic strain for an axially symmetric problem can be computed by (Britto and Gunn (1987)):

$$\delta\varepsilon_q^p = \frac{2}{3}\left(\delta\varepsilon_1 - \delta\varepsilon_2\right) \tag{37}$$

where $\varepsilon_2 = 0$, so the ratio:

$$\frac{\delta\varepsilon_v^p}{\delta\varepsilon_q^p} = \frac{3}{2} \tag{38}$$

We estimate the parameter $\eta$ from the yield stress point of the stress strain curve. At yield the maximum principal stress is approximately 2400 kPa and the minimum principal stress is approximately 1400 kPa. Solving equation (9) for $q$ gives a value of about 1000 kPa. Solving equation (8) gives $p' \approx 1700$ kPa. Solving equation (30) gives $\eta = 0.588$. We can then solve for $M$ by rearranging equation (26):

$$M = \sqrt{3\,\eta + \eta^2} \approx 1.44 \tag{39}$$

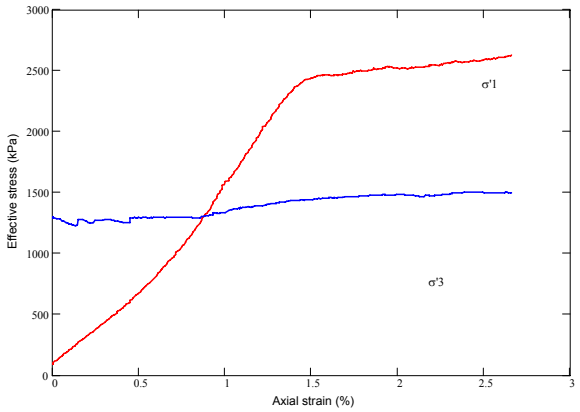


**Figure 10: Stress strain curves for $\sigma_1'$ and $\sigma_3'$ for $K_0$ triaxial test 80 from Pender, et al (2009a).**

Pender (personal communication, 4 September 2015) estimated the initial void ratio to be 0.688 and from that found the slope of $\lambda$, the normal consolidation line, to be 0.244. The final parameter $e_1$, related to the intercept of the normal consolidation line, was estimated to match the yield stress of the material. The final material parameters used for the exponential hardening model are presented in Table 1.

**Table 1: Material parameters for exponential hardening model.**

| Parameter | Value |
|---|---|
| $\kappa$ | 0.008 |
| $\nu$ | 0.08 |
| $M$ | 1.44 |
| $\lambda$ | 0.244 |
| $e_1$ | 4.2 |

### 4.3 Tabular Hardening

The tabular hardening ABAQUS model requires the use of the elastic model `*ELASTIC` with inputs of the material parameters Young's modulus ($E$) and Poisson's ratio ($\nu$). As with the exponential hardening model, Poisson's ratio was reported at 0.08. The constrained elastic modulus ($M^e$) was found by Pender to be 206 MPa (Figure 10) and is related to Young's modulus by:

$$E = \frac{M^e(1+\nu)}{(1+\nu)(1-2\nu)} \approx 203\,\text{MPa} \tag{40}$$

The additional clay plasticity parameters to determine were $M$ (equation (30)) and the table of hardening parameters $p'$ and $\varepsilon_v^p$. The first value of $p'$ for the hardening table corresponds to the mean effective yield stress as ABAQUS requires the first plastic volumetric strain to be zero. In order to simplify the use of the table, we chose to specify one additional pair of points. The second volumetric plastic strain value would be chosen to roughly correspond to the final test strain (4.0%). This meant that the total unknown parameters to calibrate for this model were three (3): $M$, $p'_y$, and $p'_f$, where the subscripts $y$ and $f$ stand for *yield* and *final* respectively.

As the stress-strain curve experiences significant softening at yield, the values of $p'_y$ and $p'_f$ needed to be very close. We chose $M$ initially to be 0.8 and increased it incrementally until a good fit was obtained. The final parameters used in the tabular hardening model are presented in Table 2.

**Table 2: Material parameters for tabular hardening model.**

| Parameter | Value |
|---|---|
| $E$ | 203 MPa |
| $\nu$ | 0.08 |
| $M$ | 1.6 |
| $p'_y$ | 2.4 MPa |
| $p'_f$ | 2.5 MPa |
| $\varepsilon^p_{v(y)}$ | 0.0 |
| $\varepsilon^p_{v(f)}$ | 0.4 |

## 5. PARAMETER STUDY

In order to improve our understanding of the effects each material parameter has on the simulation, it is necessary to perform a parameter study. In this study, the baseline material parameters were taken as similar values to the model calibrations in the previous section, but were changed slightly to have less significant figures and for small aesthetic purposes on the stress-strain plots. Then each parameter was increased and decreased in turn with the results plotted on the same plot as the baseline parameter. This enabled a direct comparison of the changes' effects on the stress-strain curve and will provide a useful future reference as we move on in subsidence model calibration.

### 5.1 Exponential Hardening

In the exponential hardening model, the five (5) parameters investigated with their baseline values and the high and low values tested are presented in Table 3. Figures 11-15 display the stress-strain curves with varying $\kappa$, $\nu$, $M$, $e_1$, and $\lambda$ in that order. In Figure 11, changing the elastic logarithmic bulk modulus $\kappa$ affected the elastic portion of the stress strain curve only. Recall that $\kappa$ is defined as the slope of the loading/unloading line on the $\ln(p') - \mathcal{V}$ plot, so a lower $\kappa$ results in a stiffer elastic response of the material. In Figure 12, the Poisson's ratio $\nu$ was

varied. Poisson's ratio has little effect on the stress-strain behaviour in these triaxial tests. Interestingly a higher $\nu$ seems to result in a slightly softer elastic response. In Figure 13, the slope of the critical state line $M$ was varied. A higher $M$ results in a larger yield surface ellipse (recall Figure 5) which results in a higher yield stress by increasing the height of the yield surface ellipse. In Figure 14, the intercept $e_1$ of the critical state line in $e - \ln(p')$ space was varied. This intercept directly changes the intersection of the loading/unloading line with the critical state line and thus directly changes the yield stress. This behaviour is clearly seen in the figure. Further, since the space in semi-natural log, small changes in $e_1$ can lead to much larger changes in the stress. Similarly in Figure 15, the slope of the critical state line $\lambda$ was varied. Small changes in $\lambda$ have very similar effect to the stress strain response as changes in the intercept of the critical state line.

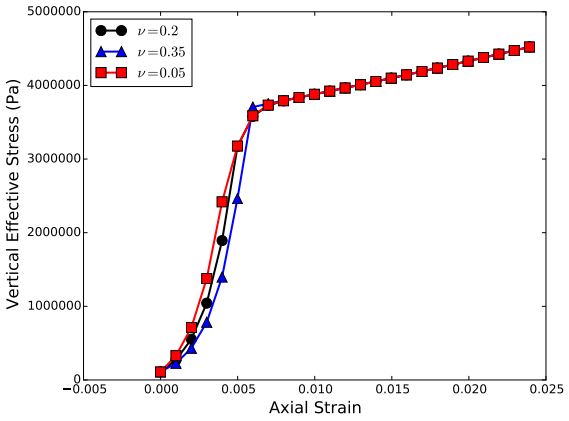


**Figure 12: Axial stress-axial strain curves for varying $\nu$ with exponential hardening model.**

**Table 3: Material parameters for exponential hardening model.**

| Param | High | Base | Low |
|---|---|---|---|
| $\kappa$ | 0.005 | 0.003 | 0.001 |
| $\nu$ | 0.35 | 0.2 | 0.05 |
| $M$ | 2.4 | 1.4 | 0.4 |
| $e_1$ | 3.0 | 2.9 | 2.8 |
| $\lambda$ | 0.16 | 0.15 | 0.14 |

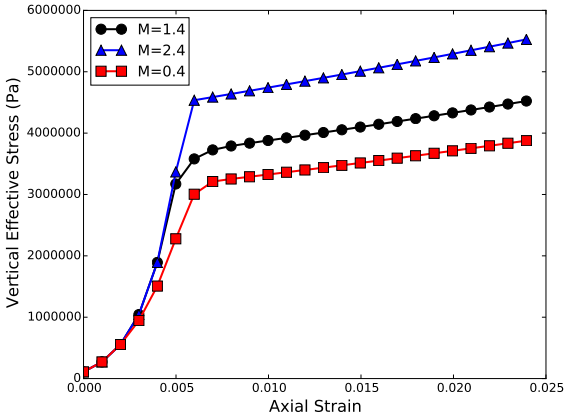


**Figure 13: Axial stress-axial strain curves for varying $M$ with exponential hardening model.**

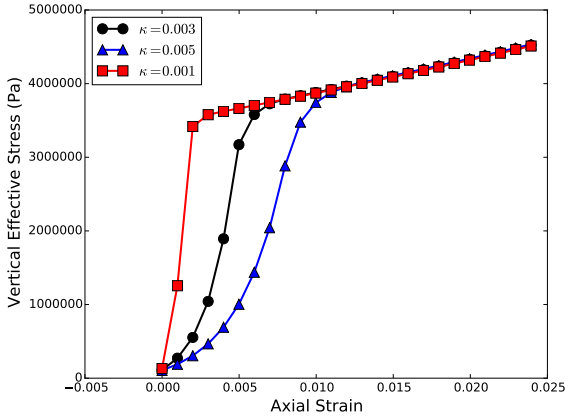


**Figure 11: Axial stress-axial strain curves for varying $\kappa$ with exponential hardening model.**

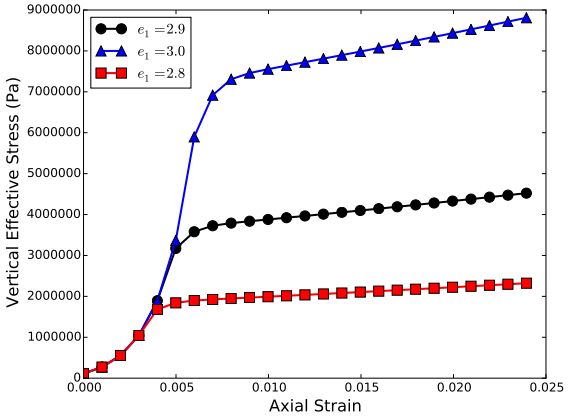


**Figure 14: Axial stress-axial strain curves for varying $e_1$ with exponential hardening model.**

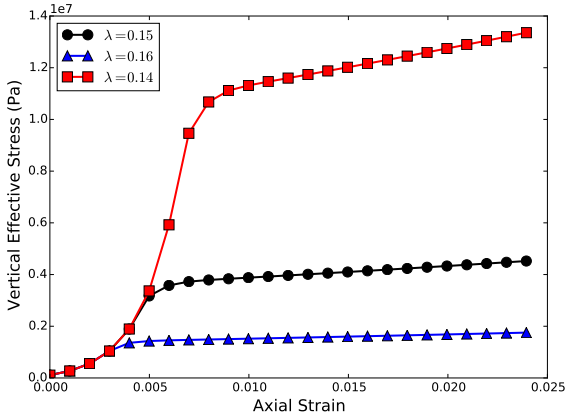


**Figure 15: Axial stress-axial strain curves for varying $\lambda$ with exponential hardening model.**

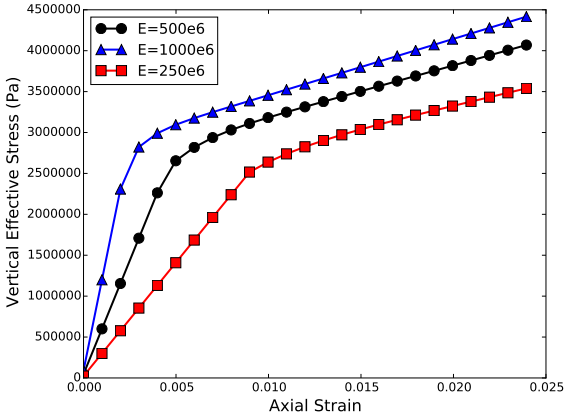


**Figure 16: Axial stress-axial strain curves for varying $E$ with tabular hardening model.**

### 5.2 Tabular Hardening

In the tabular hardening model, the five (5) parameters investigated with their baseline values and the high and low values tested are presented in Table 4. Figures 16-20 display the stress-strain curves with varying $E$, $\nu$, $M$, $p'_y$, and $p'_f$ in that order. In Figure 16, changing $E$ has obviously affected the slope of the elastic portion of the stress-strain curve, thus affecting the amount of elastic strain at the onset of yield. This strain carries over into the plastic portion of the stress-strain curve. The slopes of the plastic behaviour appear unchanged. In Figure 17, changing Poisson's ratio $\nu$ affects the stress development in the horizontal direction. This has the effect of stiffening the axial behaviour when increased (due to increased lateral support against deformation) and vice versa when decreased. This in turn has a similar effect to $E$ in the axial stress-strain curve, in that differences in elastic strain carry over to the plastic portion but the slope of the plastic curve does not appear affected. In Figure 18, the slope of the critical state line $M$ was changed. This seems to have a dramatic effect on the yield process as lower $M$ values cause yield to occur at lower stress/strain values than higher $M$ values. This is consistent with the Cam-clay yield surface ellipse seen in Figure 5 as a reduction in $M$ reduces the height of the ellipse, which in turn would reduce the yield stress and change the hardening behaviour of the material. In Figure 19, the mean effective yield stress $p'_y$ was varied. Obviously, a higher $p'_y$ results in a higher yield stress and vice versa. This also affects the slope of the plastic portion of the curve as a higher yield stress with the same $p'_f$ will reduce the slope and vice versa. Lastly, in Figure 20, the final mean effective stress $p'_f$ was varied. The curves are identical, but the stress at the final strain has changed. This has the effect of only changing the slope of the plastic portion of the stress-strain curve.

**Table 4: Material parameters for tabular hardening model.**

| Param | High | Base | Low |
|---|---|---|---|
| $E$ | 1000 MPa | 500 MPa | 250 MPa |
| $\nu$ | 0.35 | 0.2 | 0.05 |
| $M$ | 2.5 | 1.5 | 0.5 |
| $p'_y$ | 0.49 MPa | 0.25 MPa | 0.10 MPa |
| $p'_f$ | 0.26 MPa | 0.5 MPa | 1.0 MPa |

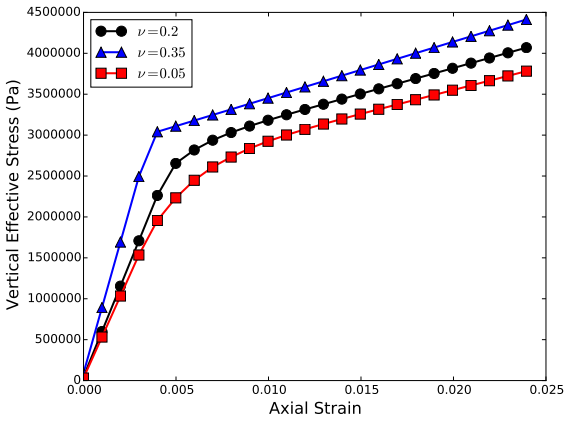


**Figure 17: Axial stress-axial strain curves for varying $\nu$ with tabular hardening model.**

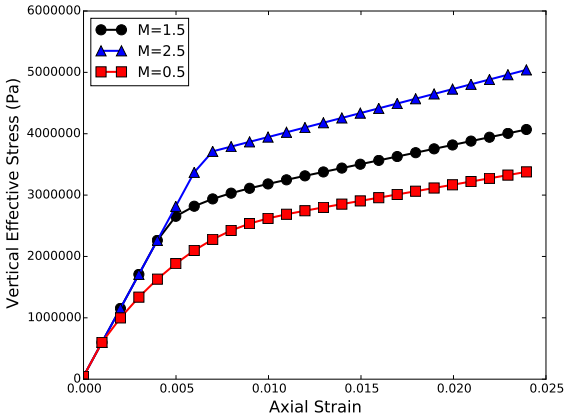


**Figure 18: Axial stress-axial strain curves for varying $M$ with tabular hardening model.**

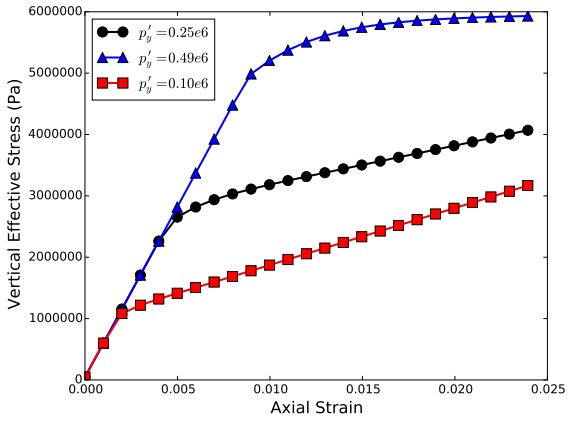


**Figure 19: Axial stress-axial strain curves for varying $p_y'$ with tabular hardening model.**

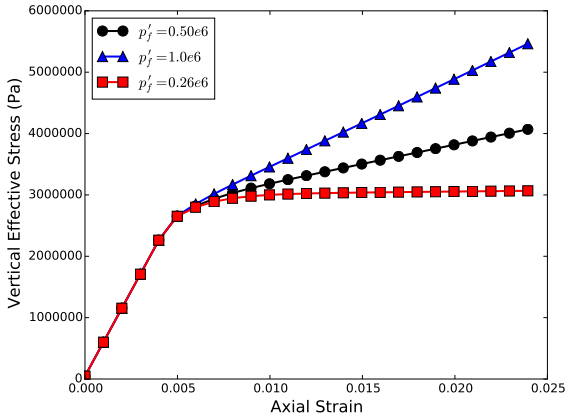


**Figure 20: Axial stress-axial strain curves for varying $p_f'$ with tabular hardening model.**

## 6. SUMMARY/CONCLUSIONS

In this work, we have outlined the theoretical development of the modified Cam-clay constitutive model. We then sought to parameterise and apply the Cam-clay model to simulate the $K_0$ triaxial test of a single well core from well THM 18. The purpose of this was to determine if the Cam-clay work hardening plasticity model could provide a suitable framework for representation of the plastic behaviour of samples within the Wairakei-Tauhara subsidence zone. The model does appear to capture the behaviour (see Figure 9). Since the goal is to apply the model to the soft zones in 1D and 3D subsidence models of the field, we then performed a parameter study on the Cam-clay parameters to better understand the exact effects each parameter has on the confined stress-strain behaviour. It is the subject of ongoing future work to determine the appropriate plasticity parameters based on triaxial and collected data from the Wairakei-Tauraha geothermal field and apply those parameters to numerical subsidence models.

## ACKNOWLEDGEMENTS

The authors gratefully acknowledge the financial support by the GRN program at GNS Science and the program director Bruce Mountain.

## REFERENCES

Allis, R.G.: Review of subsidence at Wairakei field, New Zealand. *Geothermics*, **29**, 455-478 (2000).

Allis, R.G., Zhan, X: Predicting subsidence at Wairakei and Ohaaki geothermal fields, New Zealand. *Geothermics*, **29**, 479-497 (2000).

Allis, R.G., Bromley, C., Currie, S.: Update on subsidence at the Wairakei-Tauhara geothermal system, New Zealand. *Geothermics*, **38**, 169-180 (2009).

Bonet, J., Wood, R.: *Nonlinear Continuum Mechanics for Finite Element Analysis*, Cambridge University Press, Cambridge, UK (2008).

Britto, A.M., Gunn, M.J.: *Critical State Soil Mechanics Via Finite Elements*, Ellis Horwood Ltd, Chicester, England (1987).

Bromley, C.J., Brockbank, K., Glynn-Morris, T., Rosenberg, M.D., Pender, M., O'Sullivan, M., Currie, S.: Geothermal Subsidence study at Wairakei-Tauhara. *Proceedings of the Institute of Civil Engineers. Geotechnical Engineering*, 166(2) (2013).

Bromley, C., Currie, S., Ramsay, G., Rosenberg, M., Pender, M., O'Sullivan, M., Lynne, B., Lee, S.G., Brockbank, K., Glynn-Morris, T., Mannington, W., Garvey, J.: *Tauhara Stage II Geothermal Project: Subsidence Report*, GNS Science (2010).

Chen, W.F., Han, D.J.: *Plasticity for Structural Engineers*, Gau Lih Book Co Ltd., Taiwan, R.O.C. (1995).

Gertsema, J.: Land subsidence above compacting oil and gas reservoirs. *Journal of Petroleum Technology*, 734-744 (1973).

Hatton, J.W.: Ground subsidence of a geothermal field during exploitation. *Geothermics*, Special Issue 2, 1294-1296 (1970).

Herd, M.A.: *Mathematical Modelling of Subsidence Above Geothermal Reservoirs* (ME Thesis), University of Auckland (1985).

Ingebritsen, S., Sanford, W., Neuzil, C.: *Groundwater in Geologic Processes* Cambridge University Press, New York (1999).

Koros, W., O'Sullivan, J., Pogacnik, J., O'Sullivan, M., Pender, M., Bromley, C.: Variability of Geotechnical Properties within Wairakei Subsidence Bowl, New Zealand. *Proceedings* New Zealand Geothermal Workshop (2015).

Koros, W., Pogacnik, J., O'Sullivan, M., O'Sullivan, J. Ryan, G.: Coupled One-Dimensional Subsidence Modelling Using Elastic-Plastic Rheology. *Proceedings* New Zealand Geothermal Workshop 2014, Auckland, New Zealand (2014).

Lawless, J.V., Okada, W., Terzaghi, S. and White, P.J.: New 2-D subsidence mod- elling applied to Wairakei-Tauhara. *Proceedings* New Zealand Geothermal Workshop (2001).

Lewis, R., Schrefler, B.: *The Finite Element Method in the Static and Dynamic Deformation and Consolidation of Porous Media*, John Wiley and Sons, Ltd. Chichester, England (1998).

Pender, M., Ramsay, G., Glynn-Morris, T., Lynne, B., Bromley, C.: Rock Compressibility at the Wairakei-Tauhara Geothermal Field, New Zealand, *Geotechnical Engineering*, **166** Issue GE2 (2013).

Pender, M.: *Appendix 8: Triaxial Testing of Core from the Wairakei-Tauhara Geothermal Field–Factual Procedures Report*, University of Auckland, Auckland, New Zealand (2009a).

Pender, M.: *Appendix 9: Triaxial Testing of Core from the Wairakei-Tauhara Geothermal Field–Interpretive Procedures Report*, University of Auckland, Auckland, New Zealand (2009b).

Roscoe, K.H., Schofield, A.N.: Mechanical Behaviour of an Idealised 'Wet' Clay, *Proceedings* European Conference on Soil Mechanics and Foundation Engineering, Wiesbaden, (1963).

Roscoe, K.H., Burland, J.B.: On the Generalized Behaviour of Wet Clays in Engineering Plasticity, in J. Heyman and F.A. Leckie (eds) *Engineering Plasticity*, Cambridge University Press, pp 535-609(1968).

Schrefler, B.A., Zhan, X.: A fully coupled model for water flow and airflow in deformable porous media. *Water Resources Research*, **29**, 155-167 (1993).

White, P.J., Lawless, J.V., Terzaghi, S. and Okada, W.: Advances in subsidence modelling of exploited geothermal fields. *Proceedings* World Geothermal Congress, (2005).

Yeh, A., O'Sullivan, M.: Modelling Subsidence in Geothermal Fields. *Proceedings* New Zealand Geothermal Workshop (2007).